



Full Length Article

# Catalytic effect of carbon-supported NiCoFeCuMg high-entropy alloy nanocatalysts on hydrogen storage properties of MgH<sub>2</sub>

Yafei Liu, Mengyuan Yue, Yusang Guo, Yaru Jiang, Yu Sun, Lizhuang Feng, Yijing Wang\*

Key Laboratory of Advanced Energy Materials Chemistry, Ministry of Education, Renewable Energy Conversion and Storage Center, Collaborative Innovation Center of Chemical Science and Engineering (Tianjin), College of Chemistry, Nankai University, Tianjin, 300071, PR China

Received 27 December 2023; received in revised form 29 February 2024; accepted 29 April 2024

Available online 24 May 2024

## Abstract

High entropy alloy (HEA) based materials have been extensively investigated as viable catalysts in hydrogen storage for their unique properties. Herein, we demonstrate a relatively mild synthesis strategy for constructing carbon-supported by NiCoFeCuMg HEA (NiCoFeCuMg@C) nanocatalysts by utilizing polymetallic metal-organic frameworks (MOFs) as precursors. The incorporation of prepared catalysts into MgH<sub>2</sub> greatly improved the hydrogen storage performance: the MgH<sub>2</sub>+NiCoFeCuMg@C composite can rapidly desorb 6.01 wt% H<sub>2</sub> at 325 °C, and the initial dehydrogenation temperature decreased to 167.2 °C, nearly 163.8 °C lower than that of the pure MgH<sub>2</sub>. Besides, the composite exhibits a fairly stable reversible capacity with 97% capacity retention after 20 cycles. Most importantly, *ex-situ* structural characterization reveals that the synergistic effects of the “hydrogen pump” role of Mg<sub>2</sub>Ni(Cu)/Mg<sub>2</sub>Ni(Cu)H<sub>4</sub> and “hydrogen gateway” role of Co<sub>3</sub>Fe<sub>7</sub>, as well as the excellent dispersion function of carbon material, contribute to the outstanding hydrogen storage properties of the MgH<sub>2</sub>+NiCoFeCuMg@C composite. This study provides valuable insights into the performance improvement of carbon-supported HEA catalysts in modification of MgH<sub>2</sub>.

© 2024 Chongqing University. Publishing services provided by Elsevier B.V. on behalf of KeAi Communications Co. Ltd.

This is an open access article under the CC BY-NC-ND license (<http://creativecommons.org/licenses/by-nc-nd/4.0/>)

Peer review under responsibility of Chongqing University

**Keywords:** Hydrogen storage; Magnesium hydride; High entropy alloy; Synergistic effect.

## 1. Introduction

The increasing global demand for clean and sustainable energy sources has led to a growing interest in hydrogen as a potential alternative to conventional fossil fuels. As a crucial carrier of green and low-carbon transformation, hydrogen holds great promise in the development of new energy because of its intrinsic clean nature, environmental-friendliness and renewability [1–5]. One of the key challenges in harnessing hydrogen as an energy carrier lies in its safe and efficient storage. The low density of hydrogen in its gaseous form necessitates the use of high-pressure tanks or cryogenic conditions for storage, requiring costly and impractical methods for widespread adoption. As a result, solid-state hydrogen storage has emerged as a more viable alternative due to its

high gravimetric and volumetric hydrogen storage, enhanced safety performance and higher efficiency [6,7]. In particular, magnesium hydride (MgH<sub>2</sub>), with high hydrogen storage capacity (7.6 wt%), abundant raw materials, and low cost, is considered one of the most promising hydrogen storage materials. However, the challenges lie in high thermodynamic stability and slow hydrogen absorption and desorption kinetics, which collectively constrain the practicality of hydrogen storage using MgH<sub>2</sub> [8–12].

Over the past several decades, numerous approaches have been explored to optimize the kinetic and thermodynamic properties of MgH<sub>2</sub>, such as nanosizing [13–15], alloying [16–18], catalyst doping [19–23]. Utilizing catalytic doping is regarded as an optimal approach for mitigating the limitations of MgH<sub>2</sub>. Specially, transition metals (Ti, V, Fe, Co, Ni, Cr, etc.) and compounds have been proved to be effective catalyst that could boost the capacities of MgH<sub>2</sub> [24–30]. The catalytic effect of ultrafine Ni nanoparticles

\* Corresponding author.

E-mail address: [wangyj@nankai.edu.cn](mailto:wangyj@nankai.edu.cn) (Y. Wang).

on the hydrogen storage  $\text{MgH}_2$  was studied by Wang et al. [31]. The improved hydrogen storage performance of composite was ascribed to the in situ formed  $\text{Mg}_2\text{Ni}/\text{Mg}_2\text{NiH}_4$ , which functioned as a “hydrogen pump” to facilitate the dehydrogenation/hydrogenation of  $\text{MgH}_2/\text{Mg}$ . Ren’s research [25] showed that the multi-valence Ti-based catalysts favor the electron transfer between  $\text{Mg}^{2+}$  and  $\text{H}^-$ , weakening the Mg-H bond. Despite these advancements, freestanding metal nanoparticles, as well as multi-metal alloy nanoparticles, encounter a challenge with their tendency to agglomerate. To tackle this challenge, carbon materials are generally incorporated into catalysts as dispersing agents, which not only prevent agglomeration but also contribute to the efficient dispersion of hydrogen storage systems [32,33]. Zhang et al. [34] report on nickel-decorated graphene nanoplate catalysts that enable the composite to exhibit superior hydrogen storage capabilities at moderate temperatures.

As an excellent combination of transition metal and carbon sources, metal-organic frameworks (MOFs) and MOF-derived materials are considered to be promising additives for the  $\text{MgH}_2$  system, owing to their high specific surface area, porosity, and chemical tunability [35–38]. Also, the in-service stability was found to be greatly enhanced by the accompanied carbon support. Recently, Xing et al. [39] used hierarchical structure flower-like MOF derivatives assembled by  $\text{CoNi}@C$  nanoparticles to improve the hydrogen storage performance of  $\text{MgH}_2$ . They suggested that the hydrogen storage performance of  $\text{MgH}_2$  improved due to the  $\text{Mg}_2\text{Co}$  and  $\text{Mg}_2\text{Ni}$  synergistic catalytic and “double hydrogen pump” effect as well as the versatility of carbon, which were formed on the surface of  $\text{Mg}/\text{MgH}_2$  particles.

Moreover, compared with the single transition metal catalyst, the multiphase and multiscale catalytic systems with diversified TMs exhibited superior catalytic effect on the hydrogen storage performance of  $\text{MgH}_2$  [40–44]. For instance, Fu et al. [41] discovered that a bimetallic  $\text{NiFe}$  alloy, supported by bamboo-like carbon nanotubes, leverages the synergistic effect between  $\alpha\text{-Fe}$  and  $\text{Mg}_2\text{Ni}/\text{Mg}_2\text{NiH}_4$  to significantly enhance hydrogenation kinetics. Similarly, the  $\text{FeCoS}@C$  catalyst was found to effectively boost the hydrogen storage kinetics through a multiphase catalytic system that includes  $\text{Mg}_2\text{Co}$ ,  $\alpha\text{-Fe}$ ,  $\text{Co}_3\text{Fe}_7$ ,  $\text{MgS}$ , and the carbon skeleton [43]. Notably, due to the exceptional physicochemical properties and synergistic catalysis among multiple elements, high-entropy alloys HEAs nanoparticles have recently garnered considerable attention in energy and catalytic applications. It is reported by Wan et al. [44] that the  $\text{FeCoNiCrMn}$  HEA can realize the synergistic mechanism of catalytic activity and the “hydrogen pump” mechanism through the formation of  $\text{Mg}_2\text{Ni}$  and  $\text{Mg}_2\text{Co}$ . In addition, the multiphase interface formed between  $\text{Mg}_2\text{Ni}/\text{Mg}_2\text{Co}$  and HEA nanoparticles can provide more nucleation sites for the formation of hydrides, which improves the hydrogenation process.

In light of the above consideration, we present a facile and scalable synthesis method for the  $\text{NiCoFeCuMg HEA}@C$  catalyst from the polycrystalline metal-organic framework, utilizing a straightforward precipitation route followed by pyroly-

sis. Diverging from the conventional solvothermal method, the MOF precursors were obtained through a room temperature precipitation reaction in the aqueous phase, thereby reducing or eliminating the need for organic solvents. This approach not only brings about green chemical benefits but also reduces costs, rendering it highly suitable for practical applications. The prepared  $\text{NiCoFeCuMg}@C$  was incorporated into  $\text{MgH}_2$  through ball milling, leading to composites with superior hydrogen desorption kinetics and exceptional cycling stability. Furthermore, we have elucidated the evolution of  $\text{NiCoFeCuMg}@C$  during hydrogen absorption/desorption and the beneficial effects on the  $\text{Mg}/\text{MgH}_2$  system through phase and microstructure characterization.

## 2. Experimental section

### 2.1. Chemicals and Reagents

Nickel nitrate hexahydrate ( $\text{Ni}(\text{NO}_3)_2 \cdot 6\text{H}_2\text{O}$ , 99%), iron nitrate nonahydrate ( $\text{Fe}(\text{NO}_3)_3 \cdot 9\text{H}_2\text{O}$ , 99%), copper nitrate trihydrate ( $\text{Cu}(\text{NO}_3)_2 \cdot 3\text{H}_2\text{O}$ , 99%) and 2,5-dihydroxyterephthalic acid (DHTA, 98%) were purchased from Shanghai Aladdin Biochemical Technology Co., Ltd. Cobalt nitrate hexahydrate ( $\text{Co}(\text{NO}_3)_2 \cdot 6\text{H}_2\text{O}$ , 99%), magnesium nitrate hexahydrate ( $\text{Mg}(\text{NO}_3)_2 \cdot 6\text{H}_2\text{O}$ , 99%), and sodium hydroxide ( $\text{NaOH}$ , 99%) were obtained from Damas-Beta, Alfa Aesar, and Innochem, respectively. All the reagents were used without any further purification.

### 2.2. Synthesis of $\text{NiCoFeCuMg HEA}@C$

The formation process of the  $\text{NiCoFeCuMg-MOF}$  precursor is based on a co-precipitation method at room temperature. Primarily, 0.6 mmol 2,5-dihydroxyterephthalic acid was deprotonated by 10 mL sodium hydroxide (0.24 mmol/L) fresh aqueous solution. Meanwhile, 0.309 mmol  $\text{Ni}(\text{NO}_3)_2 \cdot 6\text{H}_2\text{O}$ , 0.309 mmol  $\text{Co}(\text{NO}_3)_2 \cdot 6\text{H}_2\text{O}$ , 0.309 mmol  $\text{Mg}(\text{NO}_3)_2 \cdot 6\text{H}_2\text{O}$ , 0.225 mmol  $\text{Fe}(\text{NO}_3)_3 \cdot 9\text{H}_2\text{O}$  and 0.045 mmol  $\text{Cu}(\text{NO}_3)_2 \cdot 3\text{H}_2\text{O}$  were ultrasonically dissolved in 10 mL deionized water, which was added dropwise into the aforementioned solution. After stirring vigorously at room temperature, black precipitate was generated. The resultant precipitate was centrifuged and washed with deionized water and ethanol in sequence for 2 times. Then the  $\text{NiCoFeCuMg-MOF}$  precursor was collected by drying at 60 °C under vacuum. Finally, the  $\text{NiCoFeCuMg HEA}@C$  was obtained by calcinating pristine the  $\text{NiCoFeCuMg-MOF}$  precursor at 600 °C under  $\text{H}_2/\text{Ar}$  atmosphere for 2 h with ramp rate of 5 °C  $\text{min}^{-1}$ .

### 2.3. Preparation of nano-catalyzed $\text{MgH}_2$ composites

The  $\text{NiCoFeCuMg HEA}@C$  catalysts were doped into  $\text{MgH}_2$  using high energy ball-milling process. Prior to the addition of the catalysts,  $\text{MgH}_2$  (2 g) was pre-milled for 20 h under a hydrogen pressure of 1 Mpa. Then, as-milled  $\text{MgH}_2$  (0.18 g) was mixed with  $\text{NiCoFeCuMg HEA}@C$  catalyst

(0.02 g) by ball-milling for 4 h. The rotational speed was 400 rpm and the balls to power ratio was 60:1 by weight. For comparison, the blank nanocrystalline  $\text{MgH}_2$  was obtained using the aforementioned standard procedures. All materials handling procedures were conducted inside an argon-filled glove-box.

#### 2.4. Materials characterizations

The phase structure of the samples was analyzed using X-ray diffraction (XRD) performed on a Rigaku MiniFlex II diffractometer, employing  $\text{Cu K}\alpha$  radiation. The scan was conducted at a rate of  $4^\circ \text{ min}^{-1}$  over a  $2\theta$  range of  $5^\circ$  to  $80^\circ$ . To characterize the thermal stability of the MOF precursor, Thermo Gravimetric and Differential Thermal Analysis (TG-DTA) was carried out using a SETARAM SENSYS evo instrument. The analysis spanned a temperature range from  $25^\circ \text{C}$  to  $800^\circ \text{C}$ , with a heating rate of  $5^\circ \text{C min}^{-1}$ . The morphology and elemental distribution of samples were extensively investigated by scanning electronic microscopy (SEM, JEOL JSM-7900) and transmission electronic microscopy (TEM, FEI Talos F200X G2). X-ray photoelectron spectroscopy (XPS) was employed on a Thermo Scientific K-Alpha. The hydrogen desorption kinetics of composites was performed by differential scanning calorimetry (DSC, Q20P) at different heating rates ( $2, 5, 10$  and  $15^\circ \text{C min}^{-1}$ ). The isothermal absorption/desorption results were measured with Sieverts-type instrument Eminex-tec PCTmaster, the hydrogen

desorption measurements were carried out under 0.1 bar hydrogen pressure for desorption and 20 bar  $\text{H}_2$  for adsorption.

### 3. Results and discussion

#### 3.1. Morphology, phase and structure analysis of catalysts

Fig. 1a presents a schematic illustration of the synthetic process of NiCoFeCuMg HEA @C catalyst using a straightforward precipitation route followed by pyrolysis. The multicomponent MOF precursors were decomposed during pyrolysis, resulting in the formation of high-entropy alloy nanoparticles dispersed within a carbon matrix. To investigate the influence of annealing temperature on the formation of catalyst materials, we initially examined the structural evolution of NiCoFeCuMg@C samples prepared at different pyrolysis temperatures. The SEM image in Fig. 1b demonstrates that the NiCoFeCuMg@C sample prepared at  $600^\circ \text{C}$  (NiCoFeCuMg@C-600) exhibited a homogenous cross-linked nanoparticles morphology. The prepared NiCoFeCuMg@C-500, NiCoFeCuMg@C-700 and NiCoFeCuMg@C-800 showed similar morphologies, and the size of the nanoparticles increased gradually with the rise in pyrolysis temperature (Fig. S1).

The nanostructure of the samples was further analyzed by transmission electron microscopy (TEM). Fig. 1c demonstrates that the NiCoFeCuMg@C-600 displayed a uniform size of approximately 40 nm and was interconnected by an

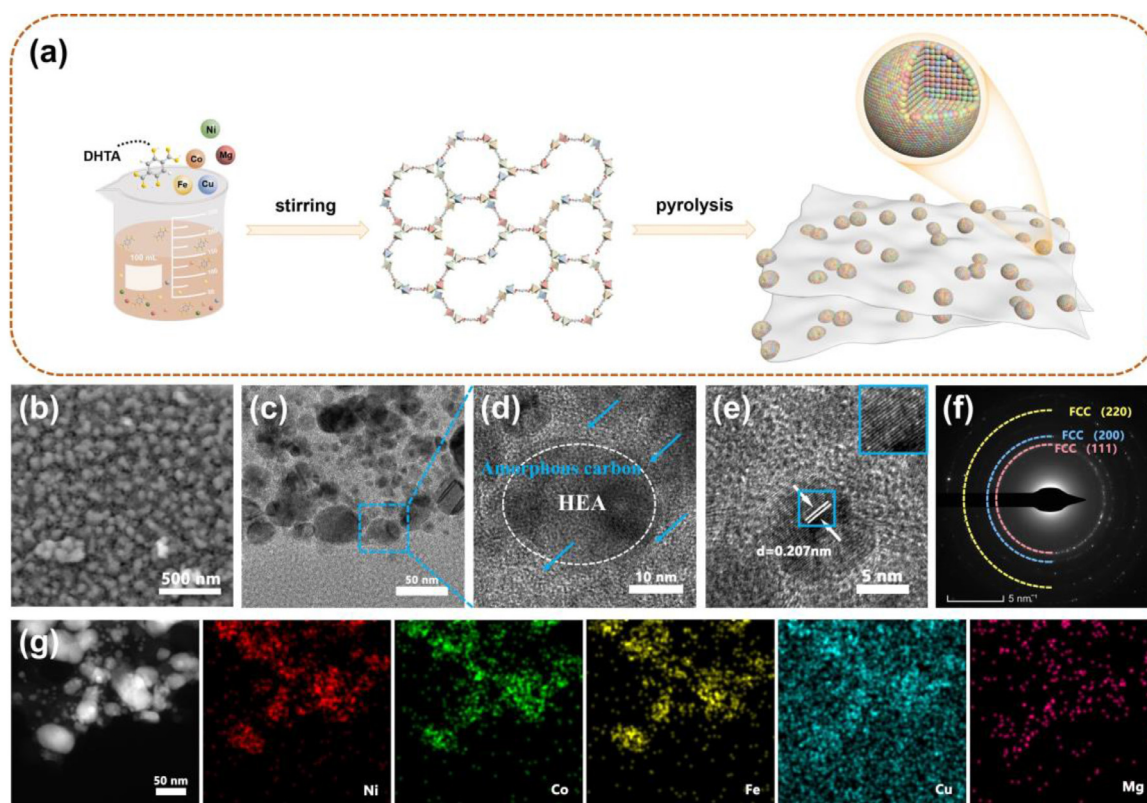


Fig. 1. (a) Schematic illustration of the facile fabrication of the NiCoFeCuMg@C catalyst. (b) SEM, (c) TEM, (d, e) HRTEM and (f) SAED of the NiCoFeCuMg@C-600. (g) HAADF image and corresponding elemental mappings of NiCoFeCuMg@C-600.



amorphous carbon layer. This carbon layer, formed through the decomposition of metal-organic frameworks (MOFs), significantly contributes to the structural integrity and functional properties of the NiCoFeCuMg HEAs. The carbon layer acts as a protective barrier, preventing the agglomeration of the high-entropy alloy nanoparticles and thus maintaining their uniform size, as observed in Fig. 1d. Furthermore, the presence of amorphous carbon introduces defects and active sites at the metal/carbon interface, which enhance the catalytic activity of the high-entropy alloy catalyst. This enhancement is crucial for reducing the activation energy required for the absorption and desorption reactions of  $\text{MgH}_2$ . The clear lattice spacing of 0.207 nm in Fig. 1e is attributed to the (111) plane of the HEA, and diffraction ring patterns of the (111), (200) and (220) crystal faces of the Face-Center Cube (FCC) could be observed in the SAED pattern of NiCoFeCuMg@C-600 shown in Fig. 1f. To reveal the element distribution of the sample, high-angle annular dark-field scanning transmission electron microscopy (HAADF-STEM) and corresponding elemental mapping images were collected. Fig. 1g displayed the homogeneous distribution of the Ni, Co, Fe, Cu and Mg, indicating that all constituent elements are intimately in contact at the nanoscale within each HEA nanoparticle. The elemental mappings of the NiCoFeCuMg@C-500, NiCoFeCuMg@C-700 and NiCoFeCuMg@C-800 samples were also analyzed, as shown in Fig. S2–S4. It can be observed that there is an even distribution of the composed elements for NiCoFeCuMg@C-700 and NiCoFeCuMg@C-800 nanoparticles. Nonetheless, samples prepared at 500 °C showed obvious internal agglomeration, which substantiated the preponderance of copper elements within these aggregated particles. This observation implies that lower calcination temperatures may induce a decelerated reaction rate during pyrolysis, resulting in insufficient interaction among different components. Consequently, this might have restricted atomic migration, thus leading to the occurrence of agglomeration phenomena.

The ligand 2,5-dihydroxyterephthalic acid exhibits characteristic peaks in the Fourier Transform Infrared Spectrometer (FTIR) at  $1650\text{ cm}^{-1}$ ,  $1498\text{ cm}^{-1}$  and  $1427\text{ cm}^{-1}$  corresponding to the vibrations of the  $\text{C}=\text{O}$  bonds, benzene ring, respectively (Figure S5). The bond at  $1180\text{ cm}^{-1}$  is assigned to the stretching vibration of  $\text{C}-\text{O}$ . In the context of multicomponent MOF precursor, these peaks experience slight shifts displacement due to a subtle redistribution of electrons caused by coordination. This spectral modification suggests the formation of coordination compounds between the ligand and metal ions, leading to alterations in the vibrational frequencies of the involved bonds. Following the application of heating treatment, no distinct characteristic peak associated with organic matter is discernible in the FTIR spectra. This observation provides evidence for the absence of organic residue in the synthesized HEA catalyst. The formation of HEA@C was characterized using X-ray diffraction (XRD). As shown in Fig. 2a and S6, the MOF precursor composite obtained through co-precipitation exhibited an amorphous structure. Upon calcination of the sample in a  $\text{H}_2/\text{Ar}$

atmosphere at 500 °C, the XRD peaks displayed broadening, and a distinct splitting peak emerged at approximately  $44.0^\circ$ , indicating a multiphase composition. Following pyrolysis at 600 °C, a significant enhancement in crystallinity was observed, resulting in a single-phase crystal structure. The XRD pattern exclusively exhibited face-center cubic (FCC) peaks, corresponding to the (111), (200) and (220) crystallographic planes of the single-phase HEA at  $43.7^\circ$ ,  $51.0^\circ$  and  $74.9^\circ$ , respectively [45,46]. Even at an elevated temperature of 700 °C and 800 °C, the XRD diffraction patterns consistently maintained a single-phase structure, aligning harmoniously with the TEM results.

The prepared sample was investigated for surface chemistry and electronic structure using X-ray photoelectron spectroscopy (XPS). The full spectrum of the NiCoFeCuMg@C-600 showed the co-existence of the Ni 2p, Co 2p, Fe 2p, Cu 2p, Mg 1s and C 1s signals (Fig. 2b). In the high-resolution Ni 2p, the peaks at 852.8 eV and 871.1 eV can be attributed to  $\text{Ni}^0\ 2p_{3/2}$  and  $\text{Ni}^0\ 2p_{1/2}$ , respectively. While the peaks at 855.5 eV and 874.7 eV correspond to  $\text{Ni}^{2+}\ 2p_{3/2}$  and  $\text{Ni}^{2+}\ 2p_{1/2}$ , accompanied by satellite peaks at 862.0 eV and 880.8 eV [47]. The high-resolution Co 2p spectrum can be deconvoluted into six peaks representing Co  $2p_{3/2}$ , Co  $2p_{1/2}$  and shake-up satellites. The peaks at 779.3 eV and 795.1 eV correspond to  $\text{Co}^0\ 2p_{3/2}$  and  $\text{Co}^0\ 2p_{1/2}$ , while the peaks at 781.8 eV and 797.1 eV can be assigned to  $\text{Co}^{2+}\ 2p_{3/2}$  and  $\text{Co}^{2+}\ 2p_{1/2}$ , along with satellite peaks at 786.9 eV and 803.8 eV [48]. As for the high-resolution Fe 2p spectrum, the peaks at 707.4 eV and 719.9 eV correspond to  $\text{Fe}^0\ 2p_{3/2}$  and  $\text{Fe}^0\ 2p_{1/2}$ , respectively. The peaks at 711.8 eV and 725.3 eV can be assigned to  $\text{Fe}^{3+}\ 2p_{3/2}$  and  $\text{Fe}^{3+}\ 2p_{1/2}$ , accompanied by satellite peaks at 715.3 eV and 733.5 eV [49]. Similarly, the high-resolution Cu 2p spectrum exhibited six peaks. The peaks at 932. eV and 951.1 eV can be assigned to  $\text{Cu}^0\ 2p_{3/2}$  and  $\text{Cu}^0\ 2p_{1/2}$ , while the peaks at 934.4 eV and 953.7 eV correspond to  $\text{Cu}^{2+}\ 2p_{3/2}$  and  $\text{Cu}^{2+}\ 2p_{1/2}$ , along with satellite peaks at 942.4 eV and 963.0 eV [50]. A characteristic peak of  $\text{Mg}^{2+}$  is observed at approximately 1303.8 eV [51]. Furthermore, the C 1s spectrum of NiCoFeCuMg@C-600 demonstrates peaks at binding energies of 284.7 eV, 286.2 eV and 289.8 eV, corresponding to C–C bonds, C–O bonds and  $\text{C}=\text{O}$  bonds, respectively [52]. These results are in accordance with the structure of designed NiCoFeCuMg HEA nanoparticles dispersed in a carbon matrix. The chemical composition of the NiCoFeCuMg@C-600 sample was investigated using ICP-OES (Table S1). Ni, Co, Fe, Cu, and Mg are present in the alloy with molar ratios of 30%, 27%, 25%, 8% and 10%, respectively. The atomic content falls within the range of 5–35%, confirming its classification as a high-entropy alloy (HEA).

### 3.2. Hydrogen storage properties of HEA@C doped $\text{MgH}_2$

The prepared catalyst was introduced into the  $\text{MgH}_2$  system through high-energy ball milling. Prior to obtaining the composite hydrogen storage material, the commercially available  $\text{MgH}_2$  underwent a 20 h pre-milling process. Figure S7 clearly illustrates the differences between untreated and pre-

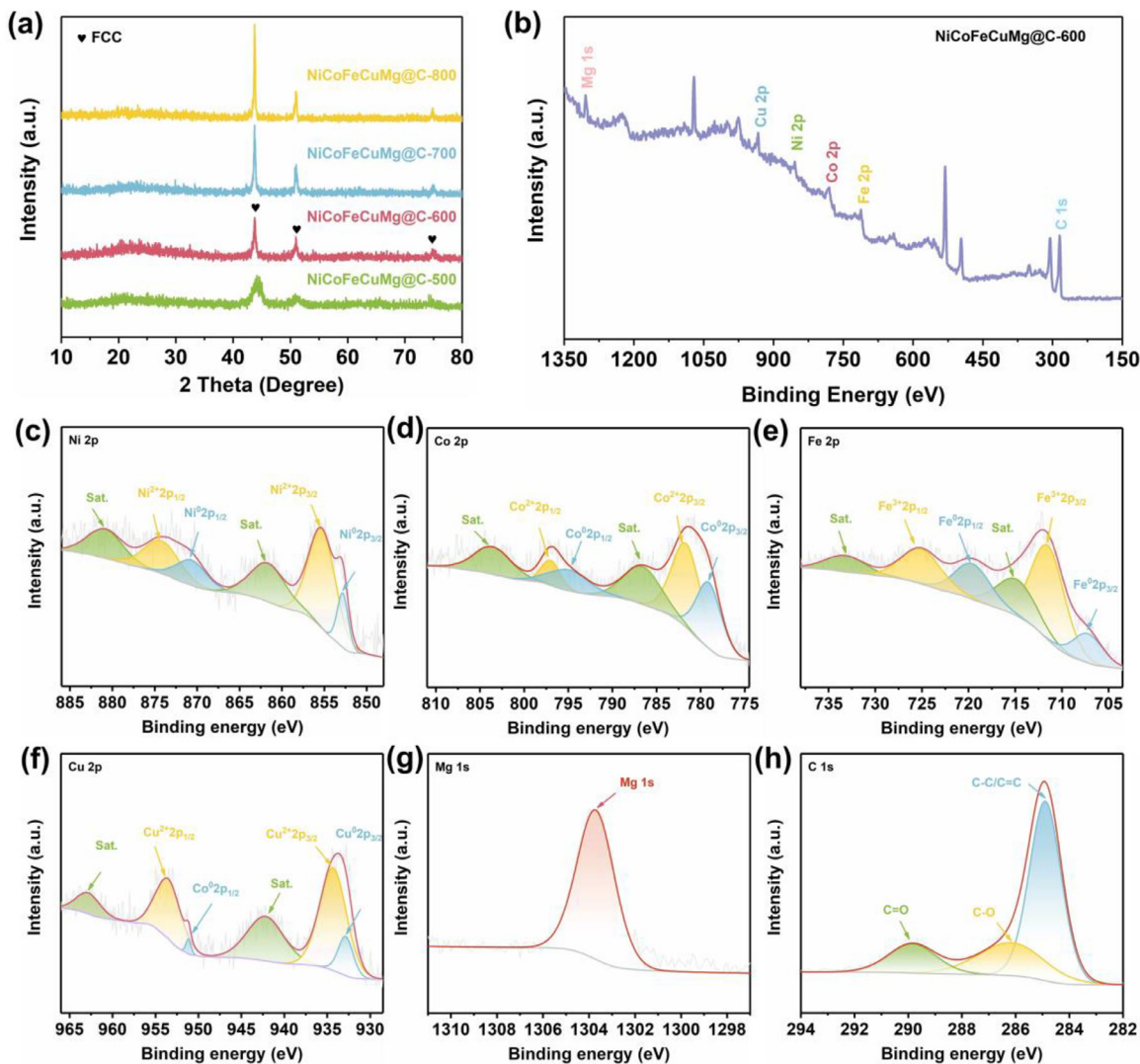


Fig. 2. (a) XRD patterns of the as prepared samples. (b) Survey XPS spectrum of NiCoFeCuMg@C-600; High-resolution XPS spectrum of (c) Ni 2p, (d) Co 2p, (e) Fe 2p, (f) Cu 2p, (g) Mg 2p and (h) C 1s.

treated  $\text{MgH}_2$ , revealing that the pre-milling treatment results in finer particle sizes and a more uniform distribution [30]. These changes are beneficial for improving the kinetics of hydrogen absorption and desorption. After pre-milling, the  $\text{MgH}_2$  was combined with the catalysts at a weight ratio of 10 wt% and subjected to a 4 h ball-milling process, resulting in the formation of hydrogen storage composites. To ensure the validity of the results, a control experiment was conducted using pure  $\text{MgH}_2$ . The control sample underwent the same ball milling procedure as the composites to mitigate any potential impact of the milling process on the catalytic performance.

To investigate the catalytic effect of HEA@C on  $\text{MgH}_2$  system, isothermal hydrogen absorption and desorption experiments were performed. The isothermal dehydrogenation curves of pure  $\text{MgH}_2$  are shown in Fig. S8. The blank  $\text{MgH}_2$  sample releases 4.40 wt%  $\text{H}_2$  in 30 min at 325 °C. At a lower temperature of 300 °C, the hydrogen desorption rate is notably reduced, reaching only 0.27 wt.% in the same period of time. Fig. 3a-c present the isothermal dehydrogenation curves of the

$\text{MgH}_2 + \text{NiCoFeCuMg@C-600}$ ,  $\text{MgH}_2 + \text{NiCoFeCuMg@C-700}$  and  $\text{MgH}_2 + \text{NiCoFeCuMg@C-800}$  composites. Compared to the pure  $\text{MgH}_2$ , these composites exhibit notable improvements in both hydrogen desorption capacity and rate at 275 °C, 300 °C and 325 °C. The detailed data comparison is shown in Table S2, showing that hydrogen release indeed increases with temperature. For instance, the  $\text{MgH}_2 + \text{NiCoFeCuMg@C-600}$  sample could release 6.06 wt%  $\text{H}_2$  within 30 min at 275 °C. Upon increasing the temperature to 300 °C, the dehydrogenation kinetics of the composites experience acceleration. The composites catalyzed by  $\text{NiCoFeCuMg@C-700}$  and  $\text{NiCoFeCuMg@C-800}$  could desorb 5.92 wt% and 4.55 wt.%  $\text{H}_2$  in 30 min, respectively. Notably, the  $\text{MgH}_2 + \text{NiCoFeCuMg@C-600}$  composite achieves 6.12 wt.% hydrogen desorption within the same time. Comparative analysis of the dehydrogenation kinetics among the three catalytic systems highlights the superior catalytic performance of  $\text{NiCoFeCuMg@C-600}$  for  $\text{MgH}_2$  dehydrogenation. At 325 °C, the  $\text{MgH}_2 + \text{NiCoFeCuMg@C-700}$

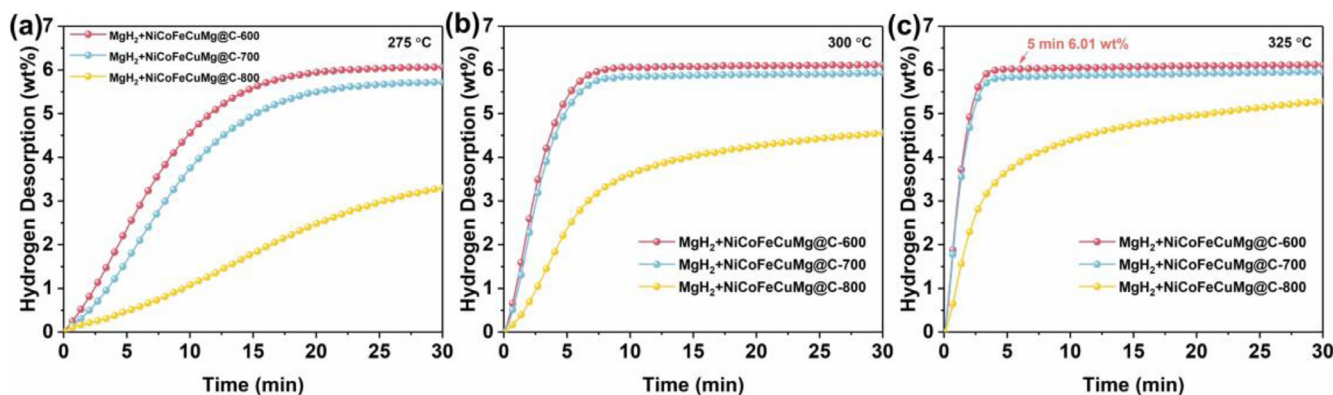


Fig. 3. Isothermal desorption curves of the  $\text{MgH}_2+\text{NiCoFeCuMg}@C-600$ ,  $\text{MgH}_2+\text{NiCoFeCuMg}@C-700$  and  $\text{MgH}_2+\text{NiCoFeCuMg}@C-800$  composites at (a) 275 °C, (b) 300 °C and (c) 325 °C.

Table 1

Comparative dehydrogenation kinetics and cycling stability of catalyzed  $\text{MgH}_2$  systems.

Samples	T/°C	t/min	Capacity/wt%	Cycle	Ref
$\text{MgH}_2\text{-CoNi}@C$	300	30	4.7	300 °C 98.7%/10 cycles	[39]
$\text{MgH}_2\text{-NiCu}@C$	300	10	5.3	275 °C 98.0%/10 cycles	[43]
$\text{MgH}_2\text{-Fe}_{0.64}\text{Ni}_{0.36}@C$	325	20	5.18	350 °C 99%/5 cycles	[53]
$\text{MgH}_2\text{-TiMgVNi}_3@C$	325	10	5.19	300 °C 92%/50 cycles	[54]
$\text{MgH}_2\text{-TiVNbZrFe}$	330	5	5.67	300 °C 94.6%/15 cycles	[55]
$\text{Mg-Ti}_{0.35}\text{V}_{0.35}\text{Nb}_{0.2}\text{Cr}_{0.1}@C$	330	8.3	6	-	[57]
$\text{MgH}_2+\text{NiCoFeCuMg}@C$	325	30	6.12	300 °C 97%/20 cycles	This study
	275	30	6.06		

and  $\text{MgH}_2+\text{NiCoFeCuMg}@C-800$  composites could release 5.96 wt% and 5.29 wt.%  $\text{H}_2$  in 30 min, respectively. In contrast, the  $\text{MgH}_2+\text{NiCoFeCuMg}@C-600$  composite rapidly desorbs 6.01 wt.%  $\text{H}_2$  within just 5 min. Table 1 presents a comparison of hydrogen storage properties of  $\text{MgH}_2$  with those of different catalysts. Among them,  $\text{MgH}_2\text{-NiCu}@C$  exhibited favorable performance, releasing approximately 5.3 wt.%  $\text{H}_2$  at 300 °C within a 10 min. Similarly, about 5.67 wt.%  $\text{H}_2$  was desorbed by the  $\text{MgH}_2\text{-TiVNbZrFe}$  composite at 330 °C for 5 min. It is worth highlighting that  $\text{NiCoFeCuMg}@C$  emerges as one of the most promising catalyst for enhancing  $\text{MgH}_2$  properties. Isothermal hydrogen absorption properties were explored on the  $\text{MgH}_2+\text{NiCoFeCuMg}@C-600$  composite, as shown in Figure S9. The exceptional kinetics of hydrogen absorption were observed under a hydrogen pressure of 2 MPa. Impressively, the composite achieved complete hydrogenation within an astonishingly short duration of 30 s at 275 °C, demonstrating exceptional hydrogen absorption dynamics. However, it is worth noting that the rapid reaction rate encountered in the hydrogenation experiments posed a challenge in accurately measuring the initial pressure. This limitation could potentially lead to an underestimation of the calculated hydrogen capacity.

Non-isothermal kinetics of the hydrogen storage composites were investigated through the differential scanning calorimetry (DSC) and temperature-programmed desorption (TPD) tests. The DSC curves in Fig. 4a demonstrated that the introduction of  $\text{NiCoFeCuMg}@C$  yielded a pronounced positive impact on reducing the dehydrogenation temperature

of  $\text{MgH}_2$ , with the  $\text{MgH}_2+\text{NiCoFeCuMg}@C-600$  composite exhibiting the most impressive dehydrogenation performance. Under a heating rate of 5 °C  $\text{min}^{-1}$ , the peak desorption temperature of pure  $\text{MgH}_2$  was determined to be 371.25 °C, whereas the  $\text{MgH}_2+\text{NiCoFeCuMg}@C-600$  composite exhibited a significantly lower dehydrogenation peak temperature of 302.96 °C. The TPD curves further validated these findings, illustrating that the  $\text{MgH}_2+\text{NiCoFeCuMg}@C-600$  composite displayed substantially lower onset and peak temperatures compared to pure  $\text{MgH}_2$  (Fig. S10). Specifically, the initial dehydrogenation temperature of the composite was measured at 167.2 °C, which was 163.8 °C lower than that of pure  $\text{MgH}_2$ , at a heating rate of 2 °C  $\text{min}^{-1}$ . Furthermore, the peak dehydrogenation temperature of the composite was observed at 289 °C, a substantial decrease compared to the peak temperature of pure  $\text{MgH}_2$  (374.8 °C).

Therefore, in comparison to the  $\text{MgH}_2+\text{NiCoFeCuMg}@C-700$  and  $\text{MgH}_2+\text{NiCoFeCuMg}@C-800$  systems, the superior hydrogen storage performance of the  $\text{MgH}_2+\text{NiCoFeCuMg}@C-600$  composite can be attributed to the following reasons: the optimal annealing temperature of 600 °C for the  $\text{NiCoFeCuMg}@C$  catalyst promotes a homogeneous nanoparticle morphology and a uniform carbon layer, which facilitates efficient hydrogen diffusion. This uniformity in particle size and the presence of amorphous carbon layer contribute to enhanced catalytic activity by providing numerous active sites for hydrogen absorption and desorption. On the other hand, the structural integrity and reduced agglomeration at this temperature allow for better dispersion of the



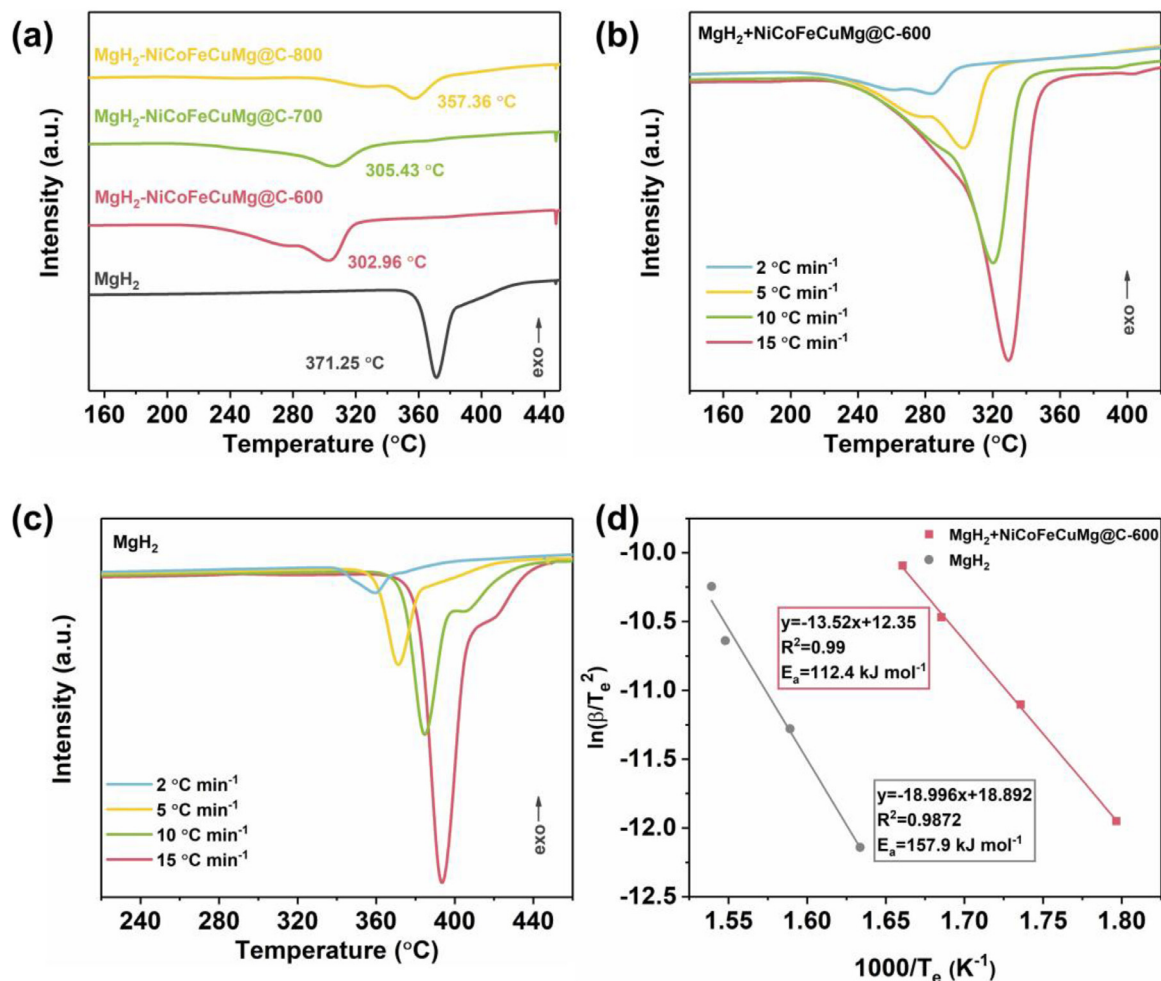


Fig. 4. (a-c) DSC curves of MgH<sub>2</sub>+NiCoFeCuMg@C-*x* (*x* = 600, 700, 800) composites at a heating rate of 5 °C min<sup>-1</sup>, (a) ball-milled MgH<sub>2</sub> (b) and MgH<sub>2</sub>+NiCoFeCuMg@C-600 (c) at different heating rate; (d) Kissinger plots for ball-milled MgH<sub>2</sub> and MgH<sub>2</sub>+NiCoFeCuMg@C-600.

catalyst within the MgH<sub>2</sub> matrix, improving the interface between MgH<sub>2</sub> and the catalyst for more effective hydrogen release. Consequently, these combined effects result in the MgH<sub>2</sub>+NiCoFeCuMg@C-600 composite exhibiting the most remarkable dehydrogenation performance, revealing the critical role of annealing temperature in tuning the catalytic performance of samples.

The apparent activation energy for hydrogen was determined through DSC curves (Fig. 4b and c). Fig. 4d displayed the Kissinger plot for the pure MgH<sub>2</sub> and MgH<sub>2</sub>+NiCoFeCuMg@C-600 composite, which was generated using the Kissinger method [56]:

$$\ln\left(\frac{\beta}{T_m^2}\right) = -\frac{E_a}{RT_m} + C$$

Here,  $T_m$  was the peak temperature,  $\beta$  was the heating rate, and the activation energy  $E_a$  could be obtained from the slope of the Kissinger plot. As a result, the apparent activation energy of MgH<sub>2</sub>+NiCoFeCuMg@C-600 was determined to be 112.4 kJ mol<sup>-1</sup>, significantly lower than the 157.9 kJ mol<sup>-1</sup> of pure MgH<sub>2</sub>. The above results provide compelling

evidence for the superior performance of NiCoFeCuMg@C in MgH<sub>2</sub> dehydrogenation.

The isothermal dehydrogenation and hydrogenation at 300 °C were performed to study the cyclic stability and reversibility of MgH<sub>2</sub>+NiCoFeCuMg@C-600 composite. The cyclic experiment involved dehydrogenation at 0.1 bar for 20 min and hydrogenation at 20 bar for 10 min. Fig. 5 illustrates the capacity retention of the composite after 20 cycles. The first isothermal dehydrogenation curve demonstrated a hydrogen release of 5.92 wt%, while even after the 20th cycle, the material retained approximately 5.75 wt% H<sub>2</sub>, resulting in an impressive capacity retention rate of 97%. In contrast, pure MgH<sub>2</sub> could achieve an initial hydrogen release of only 0.27 wt% under the same conditions, indicating poor hydrogen storage performance of pure MgH<sub>2</sub>. These results demonstrate that the MgH<sub>2</sub>+NiCoFeCuMg@C-600 composite consistently retains the capacity and kinetic performance during ab/desorption cycles. Furthermore, the utilization of SEM allowed for a more comprehensive analysis of the morphological changes of composites during hydrogen absorption and desorption, even after multiple ab/desorption cycles. In Fig. S11, it is observed that the MgH<sub>2</sub>+NiCoFeCuMg@C-

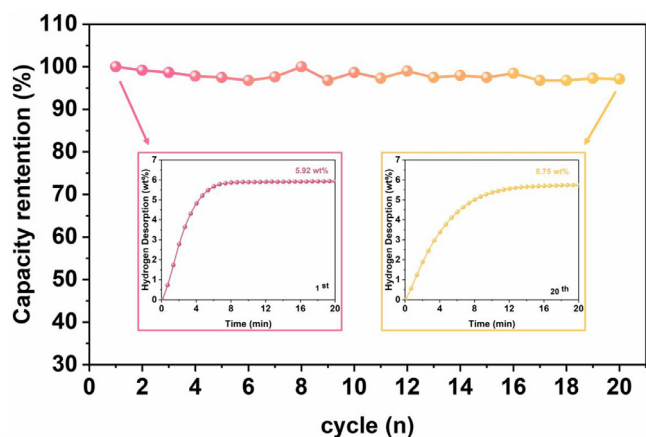


Fig. 5. Cycling capacity retention curves for  $\text{MgH}_2+\text{NiCoFeCuMg@C-600}$  with Cycle Number. The inserts present the isothermal hydrogen desorption curves for the 1st and 20th cycles.

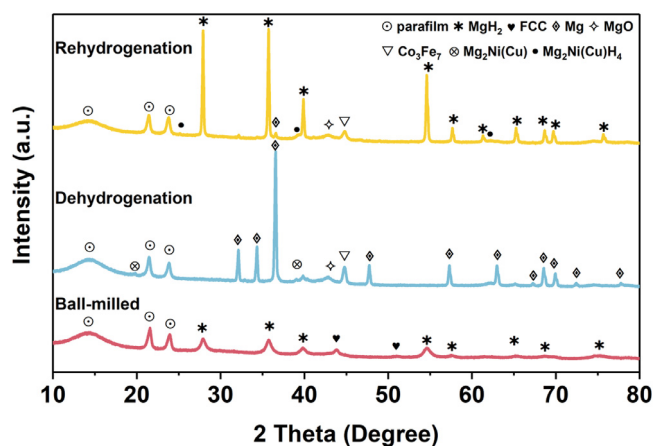


Fig. 6. XRD patterns of ball-milled, dehydrogenated and rehydrogenated  $\text{MgH}_2+\text{NiCoFeCuMg@C-600}$  composites.

600 composite maintains a consistent particle size even after multiple hydrogenation/dehydrogenation cycles. This observation strongly suggests that the presence of carbon material within the catalyst not only promotes the homogeneous dispersion of high-entropy alloy nanoparticles but effectively hinders the fragmentation and agglomeration of the  $\text{MgH}_2$  particles, thus significantly enhancing the cyclic stability of the  $\text{MgH}_2+\text{NiCoFeCuMg@C-600}$  composite.

### 3.3. Synergic catalytic mechanism

Through a comprehensive analysis of the microstructural evolution, this study further elucidates the catalytic function of the  $\text{NiCoFeCuMg@C}$  catalyst and reveals the underlying enhancement mechanism of hydrogen storage performance. Specifically focusing on the  $\text{MgH}_2+\text{NiCoFeCuMg@C-600}$  composite as a representative example, the phase evolution is meticulously investigated. Fig. 6 presents the XRD patterns of as-milled, dehydrogenated and rehydrogenated  $\text{MgH}_2+\text{NiCoFeCuMg@C-600}$  composite, enabling detailed observations of the microstructural changes. The XRD pat-

tern of the ball-milled  $\text{MgH}_2+\text{NiCoFeCuMg@C-600}$  predominantly reveals the presence of magnesium hydride and high-entropy alloy phases, indicating a straightforward physical mixing process during mechanical milling. Surprisingly, besides the transformation of the main phase into Mg after dehydrogenation, the diffraction peaks near  $20.0^\circ$  and  $40.0^\circ$  are located between the diffraction peaks of  $\text{Mg}_2\text{Ni}$  and  $\text{Mg}_2\text{Cu}$ . It is speculated that the solid solution phase  $\text{Mg}_2\text{Ni}(\text{Cu})$  is formed in situ by the combination of  $\text{NiCoFeCuMg@C}$  and  $\text{MgH}_2$  during the first dehydrogenation process. Compared with the ball-milled  $\text{MgH}_2$  sample, the rehydrogenated composite exhibited diffraction peaks of the new phase around  $23.6^\circ$ ,  $39.0^\circ$  and  $61.9^\circ$ . It is also speculated that this is related to the production of  $\text{Mg}_2\text{Ni}(\text{Cu})\text{H}_4$ , which is also consistent with previously reported results [42]. In addition, a distinct  $\text{Co}_3\text{Fe}_7$  (JCPDS No. 48–1816) signal peak emerged at  $44.7^\circ$  in the composite after hydrogen absorption, maintaining its stability throughout the de/rehydrogenation process [43]. This finding indicates the stable catalytic active substances  $\text{Co}_3\text{Fe}_7$  formed during the combination of  $\text{NiCoFeCuMg@C}$  and  $\text{MgH}_2$ . Weak  $\text{MgO}$  diffraction was also detected, which may be caused by oxidation of the sample after exposure to air during the test. Therefore, it is determined that the catalytic phases in the  $\text{MgH}_2+\text{NiCoFeCuMg@C}$  composite are the reversible  $\text{Mg}_2\text{Ni}(\text{Cu})/\text{Mg}_2\text{Ni}(\text{Cu})\text{H}_4$  and stable  $\text{Co}_3\text{Fe}_7$  phases.

The TEM, selected-area electron diffraction (SAED), high-angle annual dark-field (HADDF) and corresponding EDS mapping were employed to further explore the microstructure of the  $\text{NiCoFeCuMg@C}$  catalyzed  $\text{MgH}_2$  system. After ball-milling, dehydrogenation and rehydrogenation, the  $\text{MgH}_2+\text{NiCoFeCuMg@C}$  sample particles were observed to exhibit an irregular shape with an average particle size of approximately 500 nm, as shown in Fig. 7. Fig. 7a shows that there are some black spots scattered on the gray matrix particles. According to the EDS spectrum, Ni, Co, Fe, Cu and Mg are uniformly distributed in  $\text{MgH}_2$ . It can be inferred that the black nanoparticles correspond to high-entropy alloy catalysts doped into the  $\text{MgH}_2$  system. At the same time, the SAED patterns further confirm the presence of both  $\text{MgH}_2$  and FCC phase after ball-milling. Furthermore, the SAED patterns in Fig. 7b and c strongly support the presence of Mg,  $\text{MgO}$  and  $\text{Co}_3\text{Fe}_7$  phases during the dehydrogenation state, while the rehydrogenation state reveals the existence of  $\text{MgH}_2$ ,  $\text{MgO}$ , and  $\text{Co}_3\text{Fe}_7$  phases. It is plausible that  $\text{Mg}_2\text{Ni}(\text{Cu})$  and  $\text{Mg}_2\text{Ni}(\text{Cu})\text{H}_4$  may not be recognized in SAED analysis due to the low content and the decomposition caused by electron irradiation. Further analysis of the elemental distribution in Fig. 7b and c reveals the same distribution of Ni and Cu elements within the composites, while the distribution of Co and Fe elements also shows high consistency. These observations lend additional support to the in-situ generation of intermediate phases  $\text{Mg}_2\text{Ni}(\text{Cu})$  and  $\text{Co}_3\text{Fe}_7$ , aligning with the XRD results.

Based on the experimental results and analyses, it can be concluded that the introduction of  $\text{NiCoFeCuMg@C}$  catalyst significantly improves the hydrogen storage kinetics of  $\text{MgH}_2$ .



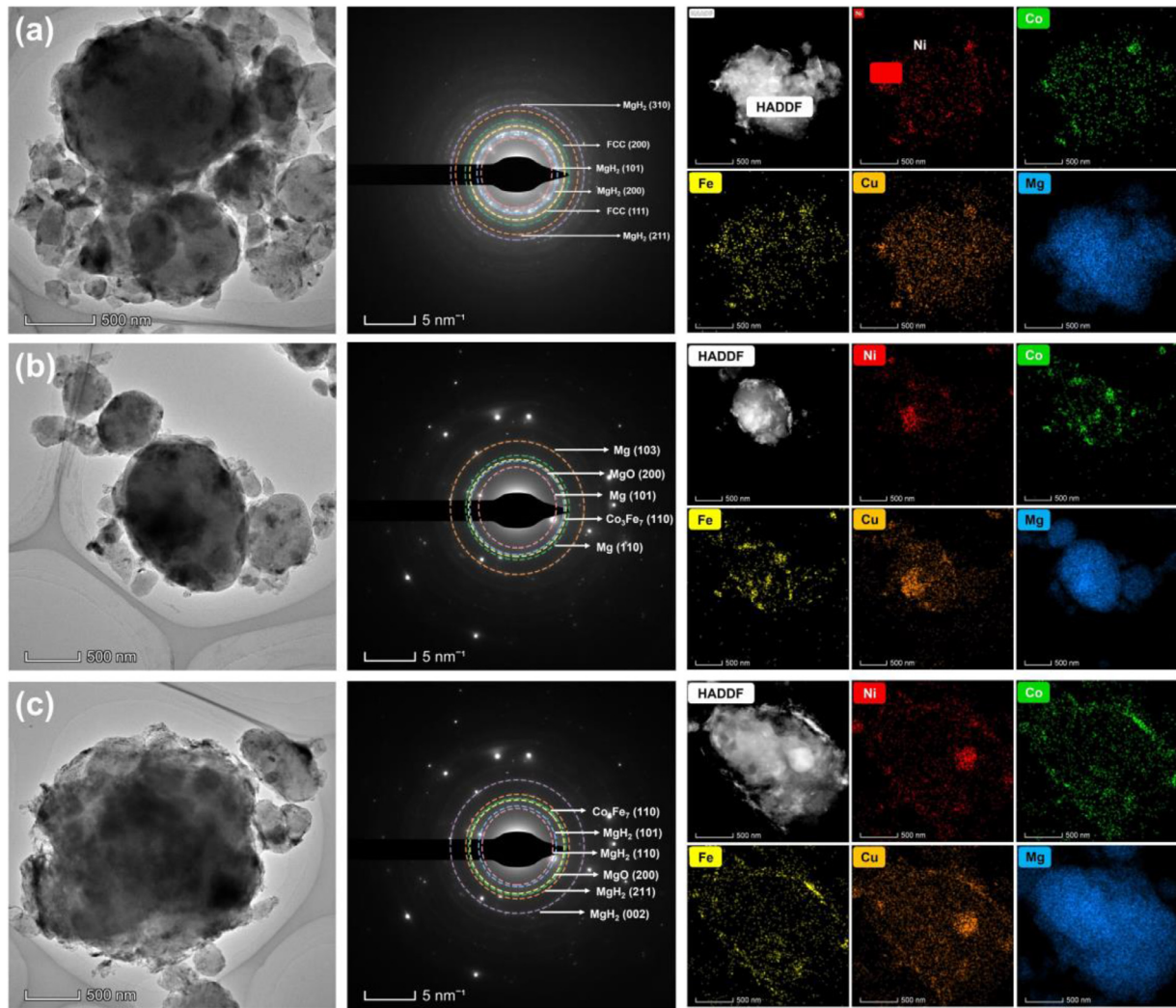


Fig. 7. The TEM images and the corresponding SAED pattern, HAADF images, corresponding EDS mapping under  $\text{MgH}_2 + \text{NiCoFeCuMg}@C\text{-600}$  composite of different states: (a) ball-milled, (b) dehydrogenated, (c) rehydrogenated.

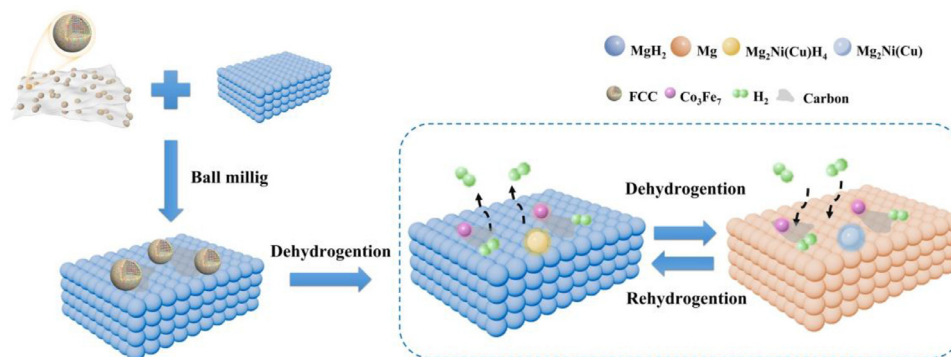


Fig. 8. Schematic diagram of the enhanced hydrogen storage performances of the  $\text{MgH}_2 + \text{NiCoFeCuMg}@C$  composites.

The catalytic mechanism was further elucidated through microstructure evolution analysis, as shown in Fig. 8. Initially,  $\text{MgH}_2$  and the  $\text{NiCoFeCuMg}@C$  catalyst were combined by high-energy ball milling, which resulted in the uniform distribution of high-entropy alloy nanoparticles in the  $\text{MgH}_2$  matrix, providing a fast channel for the rapid transfer of hydro-

gen and accelerating hydrogen diffusion. The reversible phase  $\text{Mg}_2\text{Ni}(\text{Cu})/\text{Mg}_2\text{Ni}(\text{Cu})\text{H}_4$  is formed in situ during absorption and desorption process. During hydrogenation,  $\text{Mg}_2\text{Ni}(\text{Cu})$  exhibits a lower hydrogen barrier, effectively capturing hydrogen and facilitating the formation of  $\text{Mg}_2\text{Ni}(\text{Cu})\text{H}_4$ . This phase acts as “hydrogen pump”, promoting rapid hydrogen

transfer and thus accelerating the hydrogenation of magnesium. In the dehydrogenation process,  $\text{Mg}_2\text{Ni}(\text{Cu})\text{H}_4$  decomposes back to  $\text{Mg}_2\text{Ni}(\text{Cu})$ , which then captures H from  $\text{MgH}_2$  more efficiently, speeding up the desorption process [57,58]. The  $\text{Co}_3\text{Fe}_7$  catalyst provides “hydrogen diffusion channel” through the d-electron orbitals of transition metals, accelerating hydrogen transfer [59]. Meanwhile, the carbon material coated with  $\text{Mg}/\text{MgH}_2$  plays a vital role in the system by efficiently dispersing the entire hydrogen storage system, preventing particle agglomeration, and enhancing overall performance [60]. Thus, the cycle stability and hydrogen absorption and desorption kinetics of  $\text{MgH}_2$  are greatly enhanced. Consequently, the hydrogen storage performance of  $\text{MgH}_2$  was significantly enhanced due to the synergistic effect among  $\text{Mg}_2\text{Ni}(\text{Cu})/\text{Mg}_2\text{Ni}(\text{Cu})\text{H}_4$ ,  $\text{Co}_3\text{Fe}_7$  and the carbon material.

#### 4. Conclusion

In this study, a novel cost-effective approach was developed to synthesize nanosized HEA-based catalysts from polymetallic MOF precursor. The resulting  $\text{NiCoFeCuMg}$  HEA with a face-centered cubic structure was interconnected by an amorphous carbon layer formed through precursor decomposition. When incorporated into  $\text{MgH}_2$ , the formed composites demonstrated impressive hydrogen storage performance, exhibiting an initial dehydrogenation temperature of 167.2 °C, significantly lower than that of pure  $\text{MgH}_2$  (331.0 °C). Following the isothermal kinetic test, the  $\text{MgH}_2+\text{NiCoFeCuMg}@C-600$  composite released 6.01 wt%  $\text{H}_2$  at 325 °C in 5 min. Additionally, the  $\text{MgH}_2+\text{NiCoFeCuMg}@C-600$  composite had excellent stability during hydrogen absorption and desorption cycles, with 97% capacity retention at 300 °C after 20 cycles. The improved hydrogen desorption kinetics of  $\text{MgH}_2$  can be attributed to the in-situ decomposition of the composites during the process of hydrogen absorption and desorption, leading to the formation of a multi-component catalyst system. The in-situ generated  $\text{Mg}_2\text{Ni}(\text{Cu})/\text{Mg}_2\text{Ni}(\text{Cu})\text{H}_4$  acting as a “hydrogen pump” was uniformly formed on the surface of  $\text{MgH}_2/\text{Mg}$ . Simultaneously, the stable presence of  $\text{Co}_3\text{Fe}_7$  served as “hydrogen gateway”, facilitating the transfer of hydrogen. The presence of carbon materials effectively disperses the hydrogen storage system and prevents particles from agglomerating. This synergistic effect contributes to the excellent hydrogen storage properties of the  $\text{MgH}_2+\text{NiCoFeCuMg}@C$  composite. Furthermore, the synthetic technique demonstrated in the present work can be readily scaled up to fabricate high entropy alloy-based nanocatalysts for hydrogen storage materials.

#### Declaration of Competing Interest

The authors declare that they have no known competing financial interests or personal relationships that could have appeared to influence the work reported in this paper.

#### CRedit authorship contribution statement

**Yafei Liu:** Investigation. **Mengyuan Yue:** Investigation. **Yusang Guo:** Investigation. **Yaru Jiang:** Investigation. **Yu Sun:** Investigation. **Lizhuang Feng:** Investigation. **Yijing Wang:** Conceptualization.

#### Acknowledgments

This work was supported by National Key Research and Development Program of China (2021YFB4000604), National Natural Science Foundation of China (52271220), 111 Project (B12015) and the Fundamental Research Funds for the Central Universities.

#### Supplementary materials

Supplementary material associated with this article can be found, in the online version, at [doi:10.1016/j.jma.2024.04.031](https://doi.org/10.1016/j.jma.2024.04.031).

#### References

- [1] Q. Li, X.D. Peng, F.S. Pan, J. Magnes. Alloys 9 (2021) 2223–2224.
- [2] X.L. Zhang, Y.F. Liu, X. Zhang, J.J. Hu, M.X. Gao, H.G. Pan, Mater. Today Nano 9 (2020) 100064.
- [3] L.Z. Ouyang, F. Liu, H. Wang, J.W. Liu, X.S. Yang, L.X. Sun, M. Zhu, J. Alloy. Compd. 832 (2020) 154865.
- [4] O. Sarkar, R. Katakojwala, S.V. Mohan, Green. Chem. 23 (2021) 561–574.
- [5] Q. Luo, J.D. Li, B. Li, B. Liu, H.Y. Shao, Q. Li, J. Magnes. Alloys 7 (2019) 58–71.
- [6] S. Chu, A. Majumdar, Nature 488 (2012) 294–303.
- [7] H.J. Lin, Y.S. Lu, L.T. Zhang, H.Z. Liu, K. Edalati, A. Revesz, Rare Metals 41 (2022) 1797–1817.
- [8] Y.K. Fu, Z.M. Ding, S.Q. Ren, X.J. Li, S.H. Zhou, L. Zhang, W.F. Wang, L.L. Wu, Y. Li, S.M. Han, Int. J. Hydrog. Energy 45 (2020) 28154–28162.
- [9] G. Han, Y.F. Lu, H.X. Jia, Z. Ding, L. Wu, Y. Shi, G.Y. Wang, Q. Luo, Y.A. Chen, J.F. Wang, G.S. Huang, X.Y. Zhou, Q. Li, F.S. Pan, J. Magnes. Alloys 11 (2023) 3896–3925.
- [10] C.J. Webb, J. Phys. Chem. Solids 84 (2015) 96–106.
- [11] H.Y. Shao, G.B. Xin, J. Zheng, X.G. Li, E. Akiba, Nano Energy 1 (2012) 590–601.
- [12] P. Larsson, C.M. Araujo, J.A. Larsson, P. Jena, R. Ahuja, PNAS 105 (2008) 8227–8231.
- [13] W. Zhu, L. Ren, C. Lu, H. Xu, F.Z. Sun, Z.W. Ma, J.X. Zou, ACS Nano 15 (2021) 18494–18504.
- [14] M.J. Liu, S.C. Zhao, X.Z. Xiao, M. Chen, C.H. Sun, Z.D. Yao, Z.C. Hu, L.X. Chen, Nano Energy 61 (2019) 540–549.
- [15] M. Chen, M.M. Hu, X.B. Xie, T. Liu, Nanoscale 11 (2019) 10045–10055.
- [16] X. Pang, L. Ran, Y.A. Chen, Y.X. Luo, F.S. Pan, J. Magnes. Alloys 10 (3) (2022) 821–835.
- [17] J.W. Mao, T.P. Huang, S. Panda, J.X. Zou, W.J. Ding, Chem. Eng. J. 418 (2021) 129301.
- [18] C. Liu, Q. Luo, Q.F. Gu, Q. Li, K.C. Chou, J. Magnes. Alloys 10 (2022) 3250–3266.
- [19] S. Guemou, L.T. Zhang, S. Li, Y.Q. Jiang, T. Zhong, Z.C. Lu, R. Zhou, F.Y. Wu, Q. Li, J. Mater. Sci. Technol. 172 (2023) 83–93.
- [20] Y. Zhao, T. Li, H.X. Huang, T.T. Xu, B.G. Liu, B. Zhang, J.G. Yuan, Y. Wu, J. Mater. Sci. Technol. 137 (2023) 176–183.

- [21] M.J. Liu, X.Z. Xiao, S.C. Zhao, S. Saremi-Yarahmadi, M. Chen, J.G. Zheng, S.Q. Li, L.X. Chen, *Int. J. Hydrog. Energy* 44 (2019) 1059–1069.
- [22] G.H. Liu, L.X. Wang, Y.W. Hu, C.H. Sun, H.Y. Leng, Q. Li, C.Z. Wu, *J. Alloy. Compd.* 881 (2021) 160644.
- [23] Z.Q. Lan, H. Fu, R.L. Zhao, H.Z. Liu, W.Z. Zhou, H. Ning, J. Guo, *Chem. Eng. J.* 431 (2022) 133985.
- [24] B. Liu, B. Zhang, X. Chen, Y. Lv, H. Huang, J. Yuan, W. Lv, Y. Wu, *Mater. Today Nano* 17 (2022) 100168.
- [25] L. Ren, W. Zhu, Y.h. Li, X. Lin, H. Xu, F.Z. Sun, C. Lu, J.X. Zou, *Nano-Micro Lett.* 14 (2022) 144.
- [26] H.Z. Liu, C.L. Lu, X.C. Wang, L. Xu, X.T. Huang, X.H. Wang, H. Ning, Z.Q. Lan, J. Guo, *ACS Appl. Mater. Interfaces* 13 (2021) 13235–13247.
- [27] Q. Luo, Y.L. Guo, B. Liu, Y.J. Feng, J.Y. Zhang, Q. Li, K.C. Chou, *J. Mater. Sci. Technol.* 44 (2020) 171–190.
- [28] P.K. Soni, A. Bhatnagar, V. Shukla, M.A. Shaz, *Int. J. Hydrogen Energy* 47 (2022) 21391–21402.
- [29] Z.Q. Lan, X.B. Wen, L. Zeng, Z.Q. Luo, H.R. Liang, W.T. Shi, F.F. Hong, H.Z. Liu, H. Ning, W.Z. Zhou, J. Guo, *Chem. Eng. J.* 446 (2022) 137261.
- [30] Y.K. Huang, C.H. An, Q.Y. Zhang, L. Zang, H.X. Shao, Y.F. Liu, Y. Zhang, H.T. Yuan, C.Y. Wang, Y.J. Wang, *Nano Energy* 80 (2021) 105535.
- [31] S. Wang, M.X. Gao, Z.H. Yao, K.C. Xian, M.H. Wu, Y.F. Liu, W.P. Sun, H.G. Pan, *J. Magnes. Alloys* 10 (2022) 3354–3366.
- [32] C.W. Duan, Y.T. Tian, X.Y. Wang, M.M. Wu, D. Fu, Y.L. Zhang, W. Lv, Z.H. Su, Z.Y. Xue, Y. Wu, *Renew. Energy* 187 (2022) 417–427.
- [33] P.Y. Yao, Y. Jiang, Y. Liu, C.Z. Wu, K.C. Chou, T. Lyu, Q. Li, *J. Magnes. Alloy.* 8 (2020) 461–471.
- [34] J.G. Zhang, Y.F. Zhu, X.X. Zang, Q.Q. Huan, W. Su, D.L. Zhu, L.Q. Li, *J. Mater. Chem. A* 4 (2016) 2560–2570.
- [35] C.H. Wang, H.Y. Wang, R. Luo, C. Liu, J.S. Li, X.Y. Sun, J.Y. Shen, W.Q. Han, L.J. Wang, *Chem. Eng. J.* 330 (2017) 262–271.
- [36] J.J. Zhao, X. Quan, S. Chen, Y.M. Liu, H.T. Yu, *ACS Appl. Mater. Interfaces* 9 (2017) 28685–28694.
- [37] Z.X. Li, X.F. Xing, J.M. Chu, K.L. Wang, C.C. Yu, Z.T. Wei, Y.Y. Wen, H. Sun, Z.K. Wang, *Mater. Today Energy* 13 (2019) 125–133.
- [38] S.H. Wu, X.F. Xing, D. Wang, J.Z. Zhang, J.N. Chu, C.C. Yu, Z.T. Wei, M.L. Hu, X. Zhang, Z.X. Li, *ACS Sustain. Chem. Eng.* 8 (2020) 148–153.
- [39] X.F. Xing, Y.J. Liu, Z. Zhang, T. Liu, *ACS Sustainable Chem. Eng.* 11 (12) (2023) 4825–4837.
- [40] L.H. Liu, N. Li, M. Han, J.R. Han, H.Y. Liang, *Rare Metals* 41 (2022) 125–131.
- [41] Y.K. Fu, Z.C. Yu, S.Y. Guo, Y. Li, Q.M. Peng, L. Zhang, S.K. Wu, S.M. Han, *Chem. Eng. J.* 458 (2023) 141337.
- [42] Y.Y. Z, Z.B. Liu, J.C. Liu, Y.F. Zhu, J.G. Zhang, Y.N. Liu, X.H. Hu, L.Q. Li, *J. Magnes. Alloy.* DOI: 10.1016/j.jma.2022.04.006
- [43] Y.K. Fu, L. Zhang, Y. Li, S.Y. Guo, Z.C. Yu, W.F. Wang, K.L. Ren, Q.M. Peng, S.M. Han, *J. Mater. Sci. Technol.* 138 (2023) 59–69.
- [44] H.Y. Wan, X. Yang, S.M. Zhou, L. Ran, Y.F. Lu, Y.A. Chen, J.F. Wang, F.S. Pan, *J. Mater. Sci. Technol.* 149 (2023) 88–98.
- [45] K. Huang, B.W. Zhang, J.S. Wu, T.Y. Zhang, D.D. Peng, X. Cao, Z. Zhang, Z. Li, Y.Z. Huang, *J. Mater. Chem. A* 8 (2020) 11938–11947.
- [46] Y.J. Mei, Y.B. Feng, C.X. Zhang, Y. Zhang, Q.L. Qi, J. Hu, *ACS Catal.* 12 (2022) 10808–10817.
- [47] W.K. Tang, X.F. Liu, Y. Li, Y.H. Pu, Y. Lu, Z.M. Song, Q. Wang, R.H. Yu, J.L. Shui, *Nano Res.* 13 (2020) 447–454.
- [48] Y. Lv, M.M. Han, W.B. Gong, D.D. Wang, C. Chen, G.D. Wang, H.M. Zhang, H.J. Zhao, *Angew. Chem. Int. Edit.* 59 (2020) 23521–23526.
- [49] M. Jiang, C.P. Fu, R.Q. Cheng, W. Zhang, T.Y. Liu, R.B. Wang, J. Zhang, B.D. Sun, *Adv. Sci.* 7 (2020) 000747.
- [50] Y. Ma, Y. Zhang, X. Wang, M. Fan, K. Li, T. Wang, Y. Liu, Q. Huo, Z.A. Qiao, S. Dai, *Nanoscale* 10 (2018) 5731–5737.
- [51] J.G. Smith, J. Naruse, H. Hiramatsu, D.J. Siegel, *Chem. Mater.* 29 (2017) 3152–3163.
- [52] F.Q. Chen, J.Q. Ding, K.Q. Guo, L. Yang, Z.G. Zhang, Q.W. Yang, Y.W. Yang, Z.B. Bao, Y. He, Q.L. Ren, *Angew. Chem. Int. Edit.* 60 (2021) 2431–2438.
- [53] Z.M. Ding, Y.K. Fu, L. Zhang, I.A. Rodríguez-Pérez, H.M. Zhang, W.F. Wang, Y. Li, S.M. Han, *J. Alloy. Compd.* 843 (2020) 156035.
- [54] C.D. Hu, Z.W. Zheng, T.Z. Si, Q.A. Zhang, *Int. J. Hydrog. Energy* 47 (2022) 3918–3926.
- [55] J.X. Zhang, H. Liu, C.S. Zhou, P. Sun, X.Y. Guo, Z.G.Z. Fang, *J. Mater. Chem. A* 11 (2023) 4789–4800.
- [56] H. Kissinger, *Anal. Chem.* 29 (1957) 1702–1706.
- [57] T. Si, F. Yin, X. Zhang, Q.A. Zhang, D. Liu, Y. Li, *Scr. Mater.* 222 (2023) 115052.
- [58] J.H. Zang, S.F. Wang, R.R. Hu, H. Man, J.C. Zhang, F. Wang, D.L. Sun, Y. Song, F. Fang, *J. Mater. Chem. A* 9 (2021) 8341–8349.
- [59] D. Liang, H.Z. Zhang, X.C. Ma, S.L. Liu, J.F. Mao, H.Y. Fang, J.M. Yu, Z.Q. Guo, *Mater. Today Energy* 17 (2020) 100433.
- [60] Z.Q. Lan, F.F. Hong, W.T. Shi, R.L. Zhao, R.H. Li, Y. Fan, H.Z. Liu, W.Z. Zhou, H. Ning, J. Guo, T.Z. Huang, *Chem. Eng. J.* 468 (2023) 143692.